PAPER

DNS of the spatiotemporal evolution of the vorticity in (pure) mode B of a circular cylinder's wake

To cite this article: L M Lin and Z R Tan 2022 *Fluid Dyn. Res.* **54** 015511

IOP Publishing | The Japan Society of Fluid Mechanics Fluid Dynamics Research
Fluid Dyn. Res. **54** (2022) 015511 (23pp) https://doi.org/10.1088/1873-7005/ac4ff6

DNS of the spatiotemporal evolution of the vorticity in (pure) mode B of a circular cylinder's wake

L M Lin[1] **and Z R Tan**[2,3,*]

[1] Key Laboratory for Mechanics in Fluid Solid Coupling Systems, Institute of Mechanics, Chinese Academy of Sciences, Beijing 100190, People's Republic of China
[2] School of Navigation, Wuhan University of Technology, Wuhan 430063, People's Republic of China
[3] Hubei Key Laboratory of Inland Shipping Technology, Wuhan University of Technology, Wuhan 430063, People's Republic of China

E-mail: 1084341511@qq.com

Received 23 July 2020; revised 23 January 2022
Accepted for publication 28 January 2022
Published 17 February 2022

Communicated by Professor Yasuhide Fukumoto

Abstract

In the present paper, the spatio-temporal evolution of the vorticity field in the second wake instability, i.e. (pure) mode B is investigated to understand the wake vortex dynamics and sign relationships among the three vorticity components. Direct numerical simulation of the flow past a circular cylinder in the three-dimensional (3D) wake transition is performed, typically at a Reynolds number of 300. According to the time histories of fluid forces and frequency analysis, three different stages are identified. In the fully developed wake (FDW), the spanwise vortex core is almost two-dimensional, while the vortex braid is 3D due to the dominant streamwise interaction. However, streamwise and vertical vorticities owing to the intrinsic 3D instability are already generated first on cylinder surfaces early in the computational transition (CT). The evolution of additional vorticities with the same features as mode B shows that (pure) mode B could already be formed in the late CT. In the FDW, a special sign symmetry of these additional vorticities on the rear surface is observed, which is exactly opposite to that in (pure) mode B. Similarly, the two sign laws found in (pure) mode A are also verified in three typical regions, independent of the Reynolds number, for (pure) mode B. Particularly, the mechanism for the physical origin of streamwise and vertical vortices in the shear layers is

* Author to whom any correspondence should be addressed.

the vortex generation on the wall first and then dominant vortex induction just near the wall. The entire process of the formation and shedding of vortices with three components of vorticity is first and completely illustrated. Other characteristics of the evolution of mode B are presented in detail.

Keywords: wake transition, circular cylinder, vorticity, mode B, sign law

1. Introduction

A bluff body is widely used in many engineering applications, such as suspension bridges, high architectures, flexible risers and pipelines in offshore oil platforms and heat exchangers. Flow past a bluff body is a classical and basic subject in fluid mechanics. One physical reason is the appearance of unsteady wake associated with vortices alternately shed behind a body. Resultantly, the strong unsteady fluid forces acting on a body could potentially lead to fatigue damage and even violently destroy the structural integrity. With the aim of understanding and controlling the wake vortex dynamics, a great number of studies (Karniadakis and Triantafyllou 1992, Wu and Ling 1993, Barkley and Henderson 1996, Brede *et al* 1996, Williamson 1996a, 1996b, Henderson 1997, Leweke and Williamson 1998, Persillon and Braza 1998, Ling and Chang 1999, Barkley *et al* 2000, Posdziech and Grundmann 2001, Thompson *et al* 2001, Sheard *et al* 2003, Rao *et al* 2013, Jiang *et al* 2016, 2017, Agbaglah and Mavriplis 2019, Jiang and Cheng 2019) applying many methods, including physical model testing, direct numerical simulation (DNS), and linear or non-linear stability analysis, have been published in recently decades. Comprehensive reviews on such subjects can be found in previous references (Williamson 1996a, Posdziech and Grundmann 2001).

In the three-dimensional (3D) laminar wake transition of a flow past a circular cylinder (Williamson 1996a, Leweke and Williamson 1998, Ling and Chang 1999, Thompson *et al* 2001, Jiang *et al* 2016), there are two laminar wake instabilities, i.e. modes A and B, observed at Reynolds numbers in the range from 190 to 260. The Reynolds number Re is defined based on the approaching flow velocity U_∞, the cylinder diameter D and the kinematic viscosity ν of the fluid, i.e. $Re = U_\infty D/\nu$.

These two different wake instabilities, typically manifested by the variation of Strouhal number St (non-dimensional vortex-shedding frequency) as Re increases, appear successively with their specific mechanisms and features. At the first discontinuity which is hysteretic near $Re = 180 - 194$, the first wake instability, i.e. (pure) mode A, occurs with the inception of vortex loops due to the spanwise wavy deformation of primary vortices as they are shed. Such deformation is caused by an elliptic instability of the primary vortex cores and the formation of streamwise vortex pairs (with streamwise vorticity ω_x) at a spanwise wavelength of around 3–4 diameters are resulted from Biot–Savart induction. At the second discontinuous change in the $St - Re$ relation over a range of Re from 230 to 250, the second wake instability, i.e. (pure) mode B, gradually appears due to a gradual transfer of energy from mode A shedding. Such mode B comprises finer-scale streamwise vortices, with a spanwise length scale of around one diameter. It is mainly due to a hyperbolic instability of the braid shear layer region. This mode then exists when the Reynolds number reaches approximately 260. Beyond such a Reynolds number, the particularly ordered 3D streamwise vortex structure in the near wake becomes increasingly disordered. Such instability of mode B does appear to be related to the waviness of the primary vortex as in mode A, because these vortices also deform but much more uniformly along their length. Moreover, mode A comprises streamwise vortices of one sign that are in a staggered arrangement from one braid region to the next, while mode B has an in-line arrangement of streamwise vortices of the same sign.

In addition to the two pure modes A and B, there are large intermittent low-frequency wake velocity fluctuations due to the presence of large-scale spot-like vortex dislocations in the wake transition with mode A, i.e. mode A* (mode A + vortex dislocations) (Williamson 1996a). The mode A* instability destabilizes mode B in the nonlinear interaction between the two modes (Henderson 1997). Moreover, an experimental study has revealed that the wake transition from mode A* to mode B is a gradual process with intermittent swapping between the two modes (Williamson 1996b). Therefore, the appearance of mode A* or vortex dislocations will seriously interfere with both the pure modes A and B in the 3D wake transition.

It is noted that in most of the above studies, the role of streamwise vorticity is always stressed, such as in explaining the physical origin of streamwise vortices in mode A (Williamson 1996b), the complex interaction in the vortex pattern-like mode A (Meiburg and Lasheras 1988) and the complete suppression of alternately shedding Kármán vortices by introducing geometric disturbances in the square-section cylinder (Darekar and Sherwin 2001).

On the other hand, once the wake flow, as well as the vorticity field, evolves to be 3D, not only streamwise vorticity but also vertical vorticity appear. According to careful investigations of the total suppression of Kármán vortices in the wavy square cylinder's and conical cylinder's wakes at $Re = 100$ (Lin *et al* 2010, 2018), and the physical mechanism for the generation of streamwise vortices in (pure) mode A appearing in the square cylinder's and circular cylinder's wakes (Lin *et al* 2019a, 2019b), the vertical vortices (with vertical vorticity ω_y) actually play the key role.

Additionally, an interesting physical phenomenon, two sign relationships among the three components of vorticity, in the wake of a conical cylinder has been reported (Lin *et al* 2018). These relationships also exist in the first laminar wake transition, i.e. (pure) mode A, in the flow past a circular cylinder (Lin *et al* 2019b). From the viewpoint of the vorticity sign, such a phenomenon indicates that the vortical structure in mode A is specific or prescribed, i.e. Π_- and Π_+ vortices in the upper and lower shear layers, respectively, first form synchronously along the spanwise direction in the shear layers and then shed with the spanwise vortices in the near wake. It should be explained here that in the Π vortex, the head line, '—', denotes the spanwise vortex alternatively shed from the upper or lower shear layer, while two legs, '||', denote the 'rib'-like vortex tubes, just associated with streamwise and vertical vortex pairs with opposite signs. Then, the Π_- vortex in the upper shear layer is defined by $(+|\omega_x|, +|\omega_y|, -|\omega_z|)$ at $z = \frac{1}{4}\lambda$ and $(-|\omega_x|, -|\omega_y|, -|\omega_z|)$ at $z = \frac{3}{4}\lambda$, and the Π_+ vortex in the lower shear layer is defined by $(-|\omega_x|, +|\omega_y|, +|\omega_z|)$ at $z = \frac{1}{4}\lambda$ and $(+|\omega_x|, -|\omega_y|, +|\omega_z|)$ at $z = \frac{3}{4}\lambda$, where λ is the spanwise wavelength of Π-type vortex. These specific relationships are referred to as vorticity sign laws. In particular, the first sign law shows the intrinsic relationship between the streamwise and vertical components of vorticity.

Recently, similar vorticity sign laws are also revealed by the theory of vortex-induced vortex in an external flow past a bluff body under a geometrical disturbance (Lin *et al* 2019) and an internal flow through a pipe when a secondary flow appears (Lin and Wu 2020) at low and laminar Reynolds numbers. In these works, it is further theoretically confirmed that the wall-normal vorticity, which is always zero at the wall based on the vorticity definition, away from the wall is actually induced by the wall-tangent vorticity in which the rotational direction is aligned with the local flow direction. Therefore, such vortex-induced vortex mechanism is regarded as the indirect effect of viscous forces (Lin and Wu 2020), from the viewpoint of the vorticity generation mechanism. Moreover, this vortex induction mechanism is successfully used in explaining the physical origin of streamwise vortices in the shear layers and near wake for (pure) mode A (Lin *et al* 2019a, 2019b).

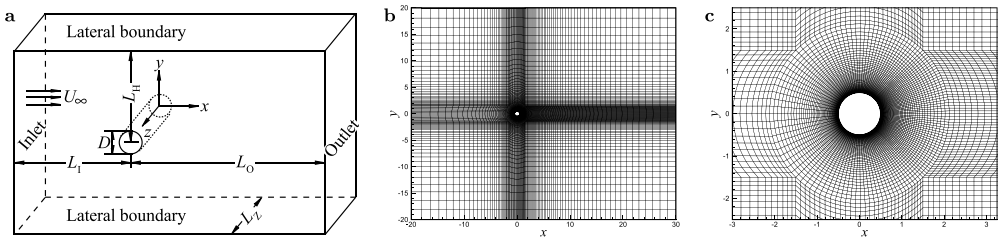

Figure 1. (a) Schematics of flow past a straight cylinder with a circular cross-section, and computational domain in the (x, y) plane and mesh distributions in (b) the whole flow region and (c) near the cylinder with a closer view.

In light of these earlier works, the primary aim of the present study, as a second part, is to investigate the spatial-temporal evolution of the vorticity, particularly including the role of the vertical vorticity or the vortex-induced vortex mechanism, and the sign relationships in (pure) mode B for a flow past a circular cylinder by means of DNS. To avoid the contamination of (pure) mode A and vortex dislocation in mode A*, (pure) mode B is investigated mainly at $Re \geqslant 300$ with the spanwise periodicity wavelength of one diameter (Williamson 1996a, Henderson 1997) and evolves from the uniform inflow as an initial flow field, rather than (pure) mode A at lower Reynolds number. The rest of this paper is organized as followings. The governing equations, boundary conditions and numerical methods are first presented. Then, based on the time histories of fluid forces, the characteristics of the spatio-temporal evolution of vorticity in different stages are mainly investigated and discussed in detail. Finally, major conclusions are given.

2. Physical model

As shown in figure 1(a), the fluid flow past a still circular-section cylinder is studied. The fluid is incompressible with constant density ρ and kinematic viscosity ν. The inertial Cartesian coordinate system is established as shown in figure 1(a), where the x axis (streamwise direction) is aligned to the incoming free stream with uniform velocity U_∞, the z axis (spanwise direction) is parallel to the cylinder span, and the y axis (vertical direction) is transverse to both the free stream and the cylinder axis.

The incompressible continuity and Navier–Stokes equations in dimensionless forms are written as

$$\nabla \cdot \boldsymbol{u} = 0, \tag{1}$$

$$\frac{\partial \boldsymbol{u}}{\partial t} + (\boldsymbol{u} \cdot \nabla)\boldsymbol{u} = -\nabla p + \frac{1}{Re}\nabla^2 \boldsymbol{u}, \tag{2}$$

where ∇ is the gradient operator, $\boldsymbol{u}$ is the velocity vector with three components (u, v, w) along their own coordinates, t is the time scaled by D/U_∞, and p is the static pressure scaled by ρU_∞^2. The velocities are scaled by the free-steam velocity U_∞ and the lengths by the cylinder diameter D. Thus, all variables used in the following context are scaled by ρ, U_∞ and D.

In the present study, some main variables and parameters are involved. The vorticity $\boldsymbol{\omega}$ is defined as the curl of velocity $\boldsymbol{u}$, i.e. $\boldsymbol{\omega} = \nabla \times \boldsymbol{u}$, with three components $(\omega_x, \omega_y, \omega_z)$ along the coordinates. As an important indicator in the present flow dynamics, variations in the drag and lift forces acting on the body are taken into account and normalized as the drag and lift

coefficients, C_D and C_L, respectively. Then, the mean drag coefficient, $\overline{C}_D$, and the root-mean-square lift coefficient, C'_L, are used to determine the intensity of fluid forces. When spanwise vortices are alternately shed in the near wake, the frequency of such vortex shedding, f, is obtained through the Fourier analysis of the time history of C_L, and scaled as the Strouhal number, St, defined by $St = fD/U_\infty$.

As for the initial condition, the flow is assumed to be still with $\boldsymbol{u} = 0$ and $p = 0$ at $t = 0$, except at the inlet.

As for the boundary conditions, the 3D flow is assumed to be spatially periodic across the span. At the inlet, the uniform free stream is prescribed as $u = U_\infty$ and $v = w = 0$. At the outlet, the simple outflow with $\partial \boldsymbol{u}/\partial x = 0$ is applied. At both lateral boundaries in the vertical direction, the free slip with velocity $\frac{\partial u}{\partial y} = v = \frac{\partial w}{\partial y} = 0$ is adopted. On cylinder surfaces, the no slip boundary condition with $\boldsymbol{u} = 0$ is used. The reference pressure of $p_\infty = 0$ is specified at the centre of the inlet.

As shown in figure 1(a), the whole non-dimensional computational domain for the present wake flow is described by the inlet length $L_I = 20$, the outlet length $L_O = 30$, the vertical height $L_H = 20$ and the computational spanwise length or cylinder span $L_Z = 1$. The blockage ratio, defined by $1/(2L_H)$, is therefore 2.5%.

The mesh distribution in the 2D computational domain is presented in figure 1(b). The smallest grid size of 0.001 is the normal distance of the first layer of the mesh next to the cylinder surface. A local mesh is mainly refined in the large circular region with a radial diameter of approximately 4.24, as shown in figure 1(c). A coarse mesh is mainly distributed far from the cylinder. The total number of the present 2D standard mesh is 20 100. The uniform spanwise grid size, $\Delta z = 0.1$, is mainly adopted.

The dimensionless time step Δt is 0.01. Here, the maximal cell Courant number, $Co = \Delta t|u|/\Delta l$, is less than approximately 0.8, where Δl is the cell size in the direction of the local velocity u through a cell.

Numerical calculations are performed using FLUENT V6.3.26 software with the finite-volume method. The pressure-implicit with splitting of operators algorithm as a pressure-velocity coupling scheme is applied. The pressure equation is solved by the second-order discretization scheme. The momentum equation adopts the second-order upwind scheme. In particular, the Green-Gauss node-based method is applied for gradient computation. The second-order implicit scheme is used in all unsteady formulations. The error of the mass conservative equation, equation (1), reaches the order of magnitude of $O(10^{-5})$, while the errors of the three components of the momentum equations, equation (2), are lower, on the order of $O(10^{-7})$.

The numerical model used here has already been validated and presented in detail in previous work (Lin *et al* 2019b). Here, the hydrodynamic parameters, $\overline{C}_D$, C'_L and St, in the present 2D simulations at different Reynolds numbers ($\leqslant$300) agree well with previous numerical calculations (Posdziech and Grundmann 2001, Jiang *et al* 2016), as summarized in table 1. However, in the 3D simulations, there is another important factor, a different computational spanwise length L_Z, compared with previous works. The effect of this factor on the evolution of the vorticity and its sign relationships will be studied in the future.

The following analysis is mainly performed at $Re = 300$. However, as a part of the independence study, the effect of the Reynolds number, i.e. $Re > 300$, on the relationship of vorticity sign and the effect of the spanwise grid size, $\Delta z = 0.05$, on the 3D vortex evolution at $Re = 300$ are also investigated. And these results are presented in the appendix. It is shown that main physical phenomena in (pure) mode B at $Re = 310$ and 320 or with $\Delta z = 0.05$ are qualitatively consistent with those at $Re = 300$.

Table 1. Summary of hydrodynamic parameters, $\overline{C}_{\mathrm{D}}$, C'_{L} and St with a frequency resolution of $\delta f = 8.3 \times 10^{-4}$, in the present 2D calculations and previous numerical results at $Re \leqslant 300$.

Re	Cases	Present	2D (Posdziech and Grundmann 2001)	2D (Jiang *et al* 2016)
270	$\overline{C}_{\mathrm{D}}$	1.3552	1.352	1.3669
	C'_{L}	0.5898	—	0.5933
	St	0.2058	0.2061	0.2065
280	$\overline{C}_{\mathrm{D}}$	1.3584	1.356	1.3701
	C'_{L}	0.6039	—	0.6067
	St	0.2075	0.2072	0.2077
300	$\overline{C}_{\mathrm{D}}$	1.3651	1.362	1.3768
	C'_{L}	0.6297	—	0.6407
	St	0.2091	0.2094	0.2107

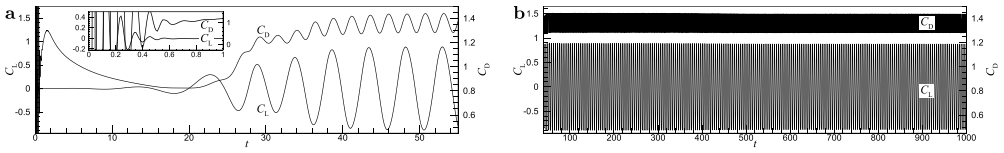

Figure 2. Time histories of C_{D} and C_{L} for (pure) mode B at $Re = 300$, typically (a) computational transition, $t \in (0, 45)$, along with a small window at $t < 1$, and (b) the stable stage with constant force amplitudes, $t > 45$.

3. Results and discussions

3.1. Time histories of fluid forces and frequency analysis

The time histories of the drag and lift coefficients for (pure) mode B at $Re = 300$ are presented in figure 2 and are obviously different from those for (pure) mode A at $Re = 200$ (Lin *et al* 2019b). It seems that there are only two main stages, the computational transition (CT) at $t < 45$ and the stable stage with almost constant oscillating amplitudes of the fluid forces, as shown in figures 2(a) and (b), respectively. For the first stage, i.e. the CT similar to that in (pure) mode A, four sub-stages are also identified. The first sub-stage (CT-1) at $t < 0.8$ corresponds to the non-physical oscillations of the fluid forces rapidly reducing as time proceeds. The second sub-stage (CT-2), at $0.8 < t < 1.5$, shows an increasing drag coefficient and a zero lift coefficient. For the third sub-stage (CT-3) at $1.5 < t < 20$, C_{D} gradually reduces to the local minimum, while the oscillating amplitude of C_{L} slowly increases when $t > 10$. The last sub-stage (CT-4) at $20 < t < 45$ is associated with C_{D} gradually increasing and oscillating when $t > 28$ and C_{L} continually increasing with oscillating amplitude.

Through Morlet wavelet analysis of the time history of C_{L}, as shown in figure 3, with a time range from 20 to 1000, only one frequency is detected, which is also different from that of (pure) mode A (Lin *et al* 2019b). Moreover, through a careful comparison of the frequency spectra for different time periods, $t < 320$ and $t > 520$, three sub-regimes in the stable stage ($t > 45$) are identified. The first two sub-regimes are the initial stage (IS), with the first at $45 < t < 320$ (IS-1) and the second at $320 < t < 520$ (IS-2). The last sub-regime is the fully developed wake (FDW) at $t > 520$, same as the second stage of FDW in (pure) mode A at $Re = 200$ (Lin *et al* 2019b).

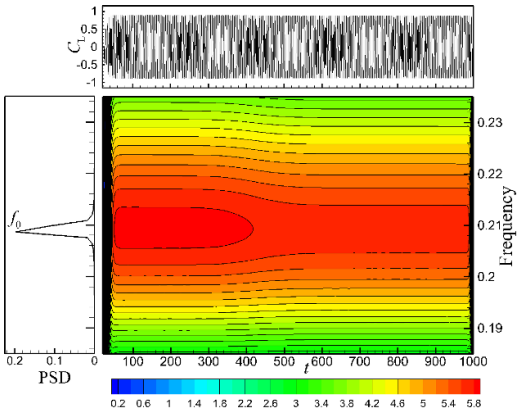

Figure 3. Frequency spectra of C_{L} obtained through Morlet wavelet analysis at $Re = 300$ with a single frequency, $f_0 = 0.2087$, at the frequency resolution of $\delta f = 1.1 \times 10^{-3}$.

Therefore, according to both the force histories and frequency analysis, there are still three main stages in the present evolution of (pure) mode B, i.e. the CT at $t < 45$, the IS at $t \in (45, 520)$ and the FDW at $t > 520$.

Here we have: $\overline{C}_{\mathrm{D}} = 1.3624$, $C'_{\mathrm{L}} = 0.6227$, and $St = 0.2087$ with $\delta f = 1.1 \times 10^{-3}$. The fluid forces in the 3D flow are slightly less than those in the 2D calculations in table 1.

3.2. *Evolution of the vorticity and its sign relationship*

In the following context, through analysis of the spatial distribution of the vorticity field at different times, three sub-regions are mainly of concern: the front surface of the cylinder denoted by 'R-I', the separated shear layers beside the body denoted by 'R-II', and the shedding primary vortices behind the body denoted by 'R-III'. Flows on and near the rear surface and in the recirculation near the wake centre plane are investigated in future. Here, only additional vorticities, ω_x and ω_y, with magnitudes of at least 0.001 are presented, avoiding possible contamination or interference caused by computational errors. The sign of the nonzero vorticity ω is defined by a sign function $\mathrm{sgn}(\omega)$ as

$$\mathrm{sgn}(\omega) = \begin{cases} 1, & \text{if } \omega > 0, \\ -1, & \text{if } \omega < 0. \end{cases} \tag{3}$$

It should be stated here that special moments or time points, as shown in figure 4, are selected at the time interval of 0.5, equal to that of saved data. The prescribed time t, associated with a certain lift coefficient at T_{i} (i = 0–4), indicates that t is approximately equal to T_{i} within the half time interval of 0.25, i.e. $|t - T_{\mathrm{i}}| < 0.25$.

3.2.1. In the CT. Except for those in the first sub-stage (CT-1), the characteristics of the (dominant) streamwise and vertical components of vorticity, as well as the spanwise vorticity, typically as shown in figure 5 at $t = 1$ and figure 6 at $t = 1.5$ in CT-2, figure 7 at $t = 10.5$ and figure 8 at $t = 20$ in CT-3, and figure 9 at $t = 41$ (T_2) in CT-4, are analysed as follows.

The wake flow, if only described by the spanwise vorticity, is almost two-dimensional throughout the entire CT. Generally, a pair of 2D spanwise vortices are first symmetrically attached on the rear surface in CT-2 (figure 5(c)), gradually elongate downstream in CT-3

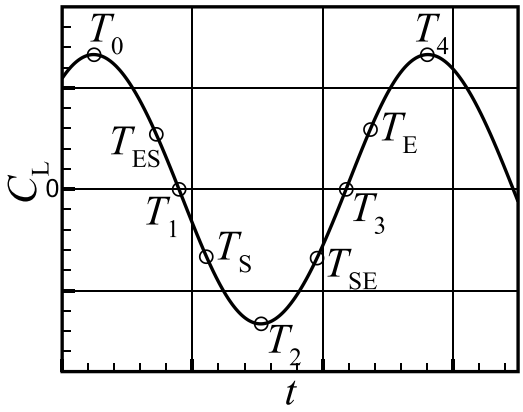

Figure 4. Typical points in a whole period or cycle of the oscillating lift coefficient, where T_0 (or T_4) and T_2 denote the positive and negative extremum values of the lift force, respectively, and both T_1 and T_3 are associated with $C_L = 0$, T_S and T_E are related to the formation of streamwise vorticity in the shear layers, and T_{SE} and T_{ES} are related to the formation of vertical vorticity in the shear layers in (pure) mode B.

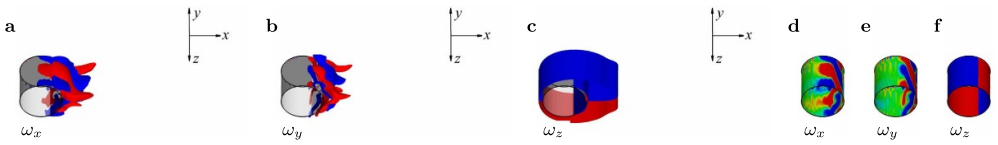

Figure 5. At $t = 1$ (CT-2), iso-surfaces of (a) $\omega_x = \pm 0.001$, (b) $\omega_y = \pm 0.001$ and (c) $\omega_z = \pm 0.1$, and contours of (d) ω_x, (e) ω_y and (f) ω_z on cylinder surfaces at $Re = 300$, where red and blue colours denote positive and negative values, respectively, and the green colour denotes values close to zero ($|\omega| < 0.001$). Note that the cylinder is denoted by the grey translucent surface among the iso-surfaces.

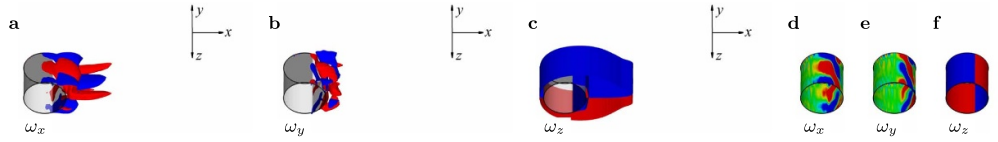

Figure 6. At $t = 1.5$ (CT-2), iso-surfaces of (a) $\omega_x = \pm 0.001$, (b) $\omega_y = \pm 0.001$ and (c) $\omega_z = \pm 0.1$, and contours of (d) ω_x, (e) ω_y and (f) ω_z on cylinder surfaces at $Re = 300$ (same descriptions as in figure 5).

until $t = 10.5$ (figure 7(c)), and then asymmetrically slightly oscillate at $t = 20$ (figure 8(c)). Finally, in CT-4, they are alternately shed from the upper and lower shear layers, i.e. Kármán vortex streets form, e.g. at $t = 41$ (figure 9(c)).

However, ω_x and ω_y appear in the wake. Initially, these additional vorticities with very small magnitudes mainly appear on the rear surface, rather than front surface at $Re = 200$ (Lin *et al* 2019b), early in the second stage (CT-2). Then, they are convected downstream into the shear layers during CT-2 and CT-3. Finally, they are alternately shed in CT-4. Moreover, these additional vorticities on the surface and in the shear layers gradually increase as time processes

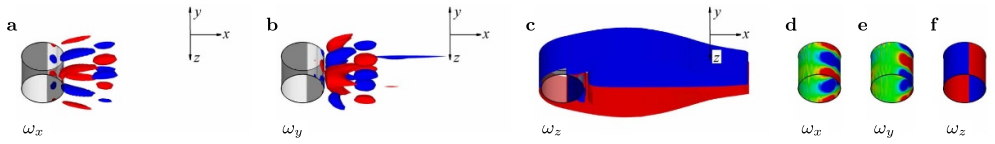

Figure 7. At $t = 10.5$ (CT-3), iso-surfaces of (a) $\omega_x = \pm 0.002$, (b) $\omega_y = \pm 0.002$ and (c) $\omega_z = \pm 0.8$, and contours of (d) ω_x, (e) ω_y and (f) ω_z on cylinder surfaces at $Re = 300$ (same descriptions as in figure 5).

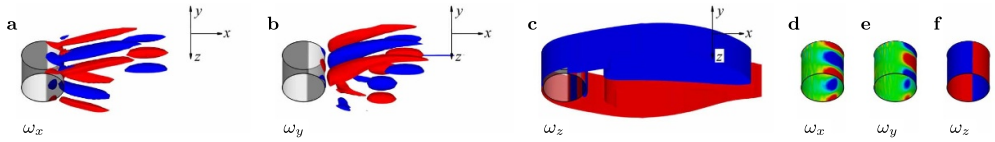

Figure 8. At $t = 20$ (CT-3), iso-surfaces of (a) $\omega_x = \pm 0.001$, (b) $\omega_y = \pm 0.002$ and (c) $\omega_z = \pm 1.5$, and contours of (d) ω_x, (e) ω_y and (f) ω_z on cylinder surfaces at $Re = 300$ (same descriptions as in figure 5).

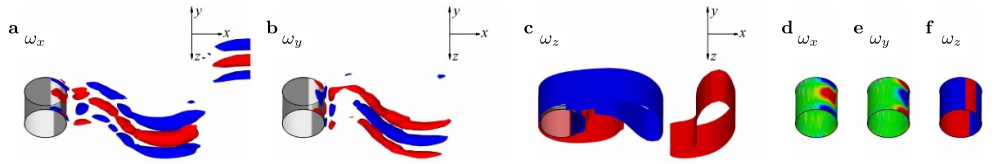

Figure 9. At $t = 41$ (CT-4, T_2), iso-surfaces of (a) $\omega_x = \pm 0.001$, (b) $\omega_y = \pm 0.001$ and (c) $\omega_z = \pm 1$, and contours of (d) ω_x, (e) ω_y and (f) ω_z on cylinder surfaces at $Re = 300$ (same descriptions as in figure 5).

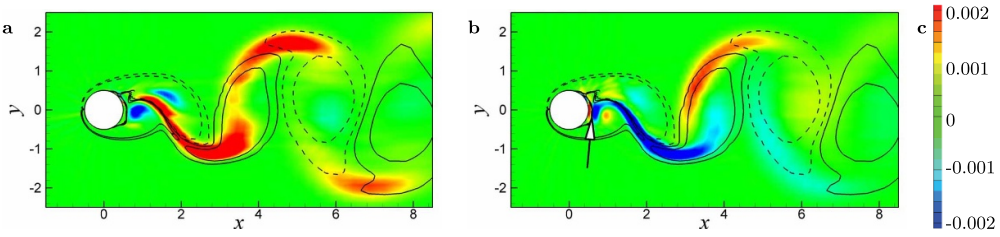

Figure 10. Colour contours of (a) ω_x and (b) ω_y at $z = 0.5$, $t = 41$ (CT-4, T_2) and $Re = 300$. In the background, only contours of $\omega_z = \pm 0.1$ and ± 0.5 are presented, where red and blue colours (also shown in the (c) colour legend for reference), as well as solid and dashed lines, denote positive and negative values, respectively. Note that the arrow with a hollow head in (b) denotes the vertical vorticity in the lower shear layer that actually does not originate from that on the lower and rear surface.

in CT-3 and CT-4. They are associated with the spanwise flow ($w \neq 0$) that first appears and then increase near cylinder walls due to the intrinsic 3D instability, similar to experiments (Yokoi and Kamemoto 1992, 1993). This result clearly indicates that the flow is actually already 3D early in the stage of CT-2, similar to that in (pure) mode A (Lin *et al* 2019b). However, the intensity is so weak that the spanwise vortices appear to be two-dimensional.

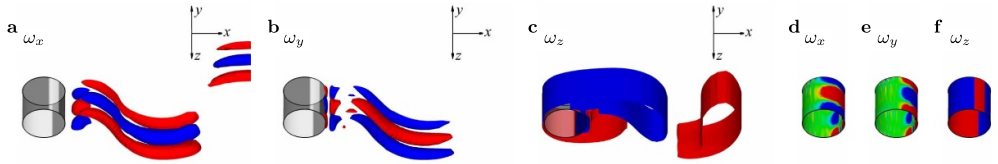

Figure 11. At $t = 256$ (IS-1, T_2), iso-surfaces of (a) $\omega_x = \pm 0.05$, (b) $\omega_y = \pm 0.05$ and (c) $\omega_z = \pm 1$, and contours of (d) ω_x, (e) ω_y and (f) ω_z on cylinder surfaces at $Re = 300$ (same descriptions as in figure 5).

In present computational conditions, the characteristic wavelength of additional vorticities is observed always to be λ not only in CT but also in IS and FDW in the subsequent context. It is associated with the Fourier mode of $n = 1$ and exactly equal to the wavelength of (pure) mode B $\lambda_B = 1$. Even so, it also indicates that the mode B instability could initially occur on and near walls at earlier moments, typically in CT-4 in figure 9 or 10.

As for the sign distributions of additional vorticities, the focus is mainly placed on sub-regions R-II and R-III because the additional vorticities in sub-region R-I almost disappear owing to the weak viscous forces at $Re = 300$. Generally, the sign of ω_x is dominantly the same as the sign of ω_y in the upper shear layer $(y > 0)$, but opposite in the lower shear layer $(y < 0)$. This reduces to the first sign law, $\mathrm{sgn}(\omega_x \cdot \omega_y) = \pm 1$ for $\pm y$. On the other hand, e.g. in CT-4, as shown in figure 10(a), the sign of the dominant ω_x is always the same in both the upper and lower shear layers and then in both vortex braid regions due to the stretching effect of the primary vortex core with the opposite sign, similar to the symmetry of mode B, i.e. an in-line arrangement from one braid region to the next (Williamson 1996a). However, as shown in figure 10(b), the sign of the dominant vertical vorticity is in a staggered arrangement in the upper and lower shear layers, similar to that in mode B of a square cylinder (Lin *et al* 2018).

Furthermore, based on the above feature, if the sign of the spanwise vorticity in sub-region R-II is taken into account, we have the interesting vorticity relationship $\mathrm{sgn}(\omega_x \cdot \omega_y \cdot \omega_z) = -1$ $(x > 0)$, referred to as the second sign law. In the R-III region, such a sign relationship is also theoretically valid for primary additional vorticities, regardless of the stretching effect. Actually, these two sign laws for vorticity components already exist early in (pure) mode A at $Re = 200$ but with a different symmetry of the additional vorticity signs in the wake (Lin *et al* 2019b).

Additionally, a type of symmetry of the dominant surface vorticities with specific signs (except near the wake centre $y = 0$) at the same spanwise position in CT-3 is discovered. $\mathrm{sgn}(\omega_x)$ on the upper side is always the same as that on the lower side, and $\mathrm{sgn}(\omega_y)$ is the opposite, typically as shown in figures 7(d) and (e), respectively. Such sign symmetry is different from that in (pure) mode A at the same sub-stage CT-3 in previous work (Lin *et al* 2019b).

3.2.2. In the IS. Some features of the vorticity and its sign when the wake evolves into the IS, as shown in figure 11 at $t = 256$ (T_2) in IS-1, and figure 12 at $t = 412.5$ (T_1) in IS-2, are analysed and summarized as follows.

In the present stage, the wake flow can still be described by the almost 2D spanwise vorticies alternately shedding, even when ω_x and ω_y increase up to approximately 0.2.

By checking additional vorticities with specific signs in sub-regions R-II and R-III at the same spanwise position, the spatial features presented in CT-4 also appear, as well as the first sign law, which are independent of the formation of spanwise vortices shed at T_1 or T_2. In

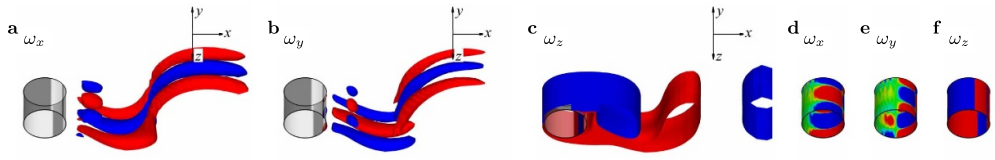

Figure 12. At $t = 412.5$ (IS-2, T_1), iso-surfaces of (a) $\omega_x = \pm 0.2$, (b) $\omega_y = \pm 0.2$ and (c) $\omega_z = \pm 1$, and contours of (d) ω_x, (e) ω_y and (f) ω_z on cylinder surfaces at $Re = 300$ (same descriptions as in figure 5).

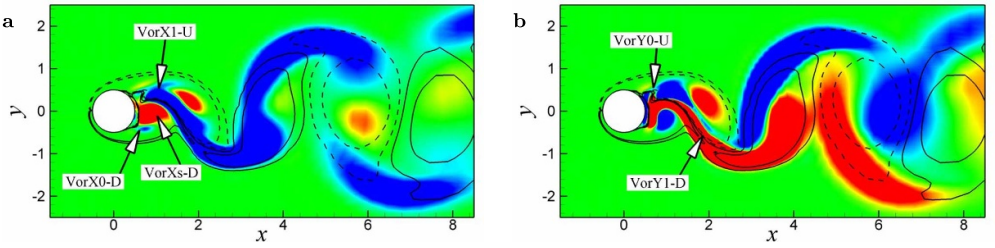

Figure 13. Colour contours of (a) ω_x and (b) ω_y at $z = 0.5$, $t = 256$ (IS-1, T_2) and $Re = 300$ (same descriptions as in figure 10).

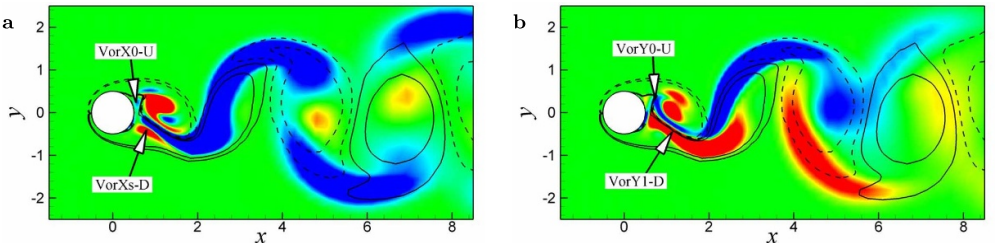

Figure 14. Colour contours of (a) ω_x and (b) ω_y at $z = 0.5$, $t = 412.5$ (IS-2, T_1) and $Re = 300$ (same descriptions as in figure 10).

sub-region R-I, as shown in figures 12(d) and (e), the first sign law is still valid, i.e. ω_x and ω_y with opposite signs are distributed on the front and lower surface.

The second sign relationship between additional vorticities and the spanwise vorticity is also obtained. In sub-region R-II, for the dominant ω_x and ω_y appearing with special spanwise vorticity, the second sign law, i.e. $\mathrm{sgn}(\omega_x \cdot \omega_y \cdot \omega_z) = -1$, is still valid. However, in sub-region R-III, such a relationship seems to be invalid near braid regions, mainly attributed to the strong stretching effect of the upstream spanwise vortex with the opposite sign on the downstream 'rib'-like vortex tubes with ω_x and ω_y. In particular, these vertical vortices are almost convected into the upstream spanwise vortex braid. For example, $+|\omega_y|$, originally shed with $+|\omega_z|$ in the lower shear layer, is moved into the braid of $-|\omega_z|$ at $x = 5$ in figure 13(b) or at $x = 4$ in figure 14(b).

As for additional components of the vorticity and their signs on the rear surface at the same spanwise position, another sign symmetry is presented, but different from the symmetrical feature in CT-3. $\mathrm{sgn}(\omega_x)$ on the rear surface is anti-symmetric about $y = 0$, but $\mathrm{sgn}(\omega_y)$ is symmetric about $y = 0$, e.g. in figures 12(d) and (e), except near the wake centre $y = 0$.

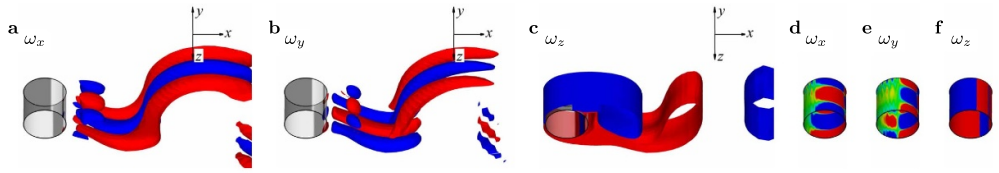

Figure 15. At $t = 843$ (T_1), iso-surfaces of (a) $\omega_x = \pm 0.2$, (b) $\omega_y = \pm 0.2$ and (c) $\omega_z = \pm 1$, and contours of (d) ω_x, (e) ω_y and (f) ω_z on cylinder surfaces at $Re = 300$ (same descriptions as in figure 5).

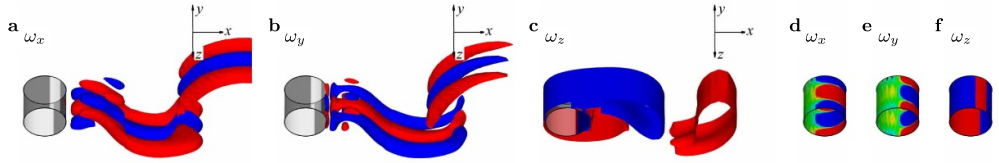

Figure 16. At $t = 844$ ($\lesssim T_2$), iso-surfaces of (a) $\omega_x = \pm 0.2$, (b) $\omega_y = \pm 0.2$ and (c) $\omega_z = \pm 1$, and contours of (d) ω_x, (e) ω_y and (f) ω_z on cylinder surfaces at $Re = 300$ (same descriptions as in figure 5).

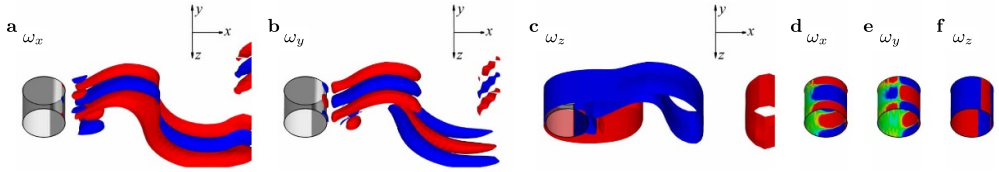

Figure 17. At $t = 931.5$ (T_3), iso-surfaces of (a) $\omega_x = \pm 0.2$, (b) $\omega_y = \pm 0.2$ and (c) $\omega_z = \pm 1$, and contours of (d) ω_x, (e) ω_y and (f) ω_z on cylinder surfaces at $Re = 300$ (same descriptions as in figure 5).

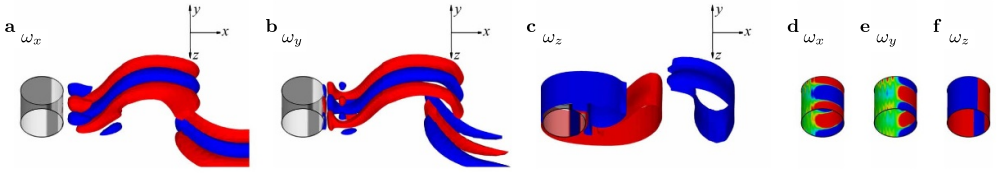

Figure 18. At $t = 932.5$ ($\lesssim T_4$), iso-surfaces of (a) $\omega_x = \pm 0.2$, (b) $\omega_y = \pm 0.2$ and (c) $\omega_z = \pm 1$, and contours of (d) ω_x, (e) ω_y and (f) ω_z on cylinder surfaces at $Re = 300$ (same descriptions as in figure 5).

3.2.3. In the FDW. The 3D wake flow is completely developed with the appearance of (pure) mode B at $t > 520$. In the present context, the flow is analysed in two half periods, i.e. ($T_0 \sim T_2$) and ($T_2 \sim T_4$), typically as shown in figure 15 at $t = 843$ (T_1) and figure 16 at $t = 844$ ($\lesssim T_2$), or in figure 17 at $t = 931.5$ (T_3) and figure 18 at $t = 932.5$ ($\lesssim T_4$), respectively.

(Pure) mode B is mainly described by alternately shedding spanwise vortices accompanied by a pair of 'rib'-like vortex tubes with streamwise and vertical vorticities of specific signs and smaller spanwise wavelengths, similar to that in (pure) mode A (Lin *et al* 2019b). In the vortex

structure of mode B, the spanwise vortex core is almost two-dimensional, but the vortex braid is a little wavy and therefore 3D, such as at $t = T_2$ or T_4. The sign of the primary streamwise vorticity is always the same in both the upper and lower shear layers at the same spanwise position, showing streamwise vortices of one sign shed in a parallel or in-line arrangement. This feature is consistent with the physical description in previous works (Williamson 1996a, 1996b). However, the signs of the dominant vertical voriticity in the upper and lower shear layers at the same spanwise position are opposite, indicating that vertical vortices of one sign shed in a staggered arrangement. This is the same phenomenon as in (pure) mode B in the wake of a square cylinder (Lin *et al* 2018). Such a feature of the specific signs of ω_x and ω_y in (pure) mode B already appeared earlier about $t = 41$ and is always dominant in R-II and R-III regimes as time passes.

Similarly, the first sign law in the above two stages still prevails in the two sub-regions R-II and R-III and even in sub-region R-I at T_1 and T_3, as shown in figures 15 and 17.

Moreover, the second sign law is also valid very precisely in sub-regions R-I and R-II for the dominant vorticity, e.g. as shown in figures 15 and 16, and theoretically valid in R-III because it stems from the shear layers.

The sign symmetry of the surface vorticities (ω_x and ω_y) on the rear surface occurring in IS always exists throughout the present stage, such as in figures 18(d) and (e).

3.3. *Physical origin of dominant* ω_x *and* ω_y *in the shear layers*

3.3.1. In the CT. The origin of ω_x and ω_y in the shear layers at the same spanwise position is analysed in CT. For example, in the upper shear layer in CT-2, $\mathrm{sgn}(\omega_x)$ is the same as that on the rear surface, e.g. in figures 5(a) and (d), which indicates that ω_x originates from that on the rear surface, similar to previous results (Yokoi and Kamemoto 1992, 1993). However, as shown in figures 5(b) and (e), opposite signs of ω_y on the rear surface and in the upper shear layer clearly show that ω_y does not originate from that on the rear surface. These phenomena also exist in CT-3 (figure 8) and CT-4 (figure 9 or 10). Based on the vortex-induced vortex mechanism reported in (pure) mode A (Lin *et al* 2019a, 2019b) and the theory (Lin *et al* 2019, Lin and Wu 2020), it can be anticipated that $+|\omega_y|$ in the upper shear layer is induced by $+|\omega_x|$ on the upper and rear surface, as a typical example in figures 8(a) and (b).

3.3.2. In the IS. When the wake flow evolves in IS, the origin of ω_x in the shear layers is first investigated. As an example, the spanwise position at $z = 0.5$ is discussed as follows. At a typical instant T_2, as shown in figures 11 and 13(a), the dominant streamwise vorticity with a negative sign in the upper shear layer (up), denoted by 'VorX1_U' in figure 13(a), may not originate from that on the rear and upper surface because of the opposite sign. However, $-|\omega_x|$ initially appearing in the lower shear layer (down), denoted by 'VorX0_D' in figure 13(a), originates from that on the lower and rear surface (in figure 11(d)), which is consistent with previous work (Yokoi and Kamemoto 1992, 1993). At T_1, as shown in figures 12(a), (d) and 14(a), $-|\omega_x|$ in the upper shear layer, denoted by 'VorX0_U' in figure 14(a), certainly originates from that generated on the lower and rear surface, which is stretched upward by the clockwise spanwise vortex in the upper shear layer. Consequently, it is anticipated that 'VorX1_U' at T_2 is actually evolved from 'VorX0_U' at T_1 and accumulates as time passes beyond T_1.

Then, the origin of ω_y in the shear layers for the present cases in figures 13(b) and 14(b) is discussed. The dominant vertical vorticity in the lower shear layer (down), denoted by 'VorY1_D', seems to not originate from that generated on the rear surface. However, it is found that the vertical vorticity in the upper shear layer (up), denoted by 'VorY0_U', really

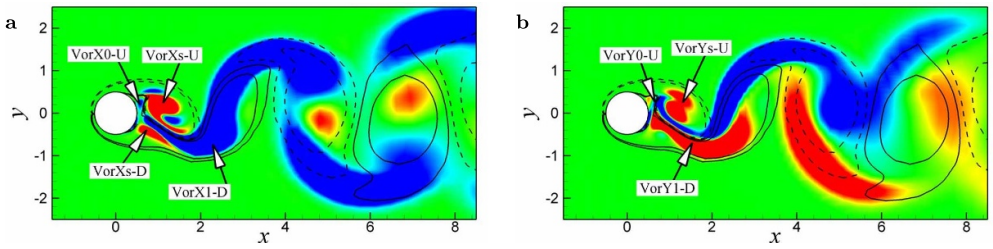

Figure 19. Colour contours of (a) ω_x and (b) ω_y at $z = 0.5$, $t = 843$ (T_1) and $Re = 300$ (same descriptions as in figure 10).

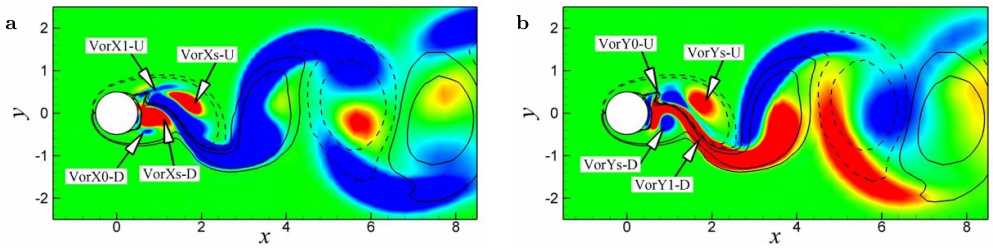

Figure 20. Colour contours of (a) ω_x and (b) ω_y at $z = 0.5$, $t = 844$ ($\lesssim T_2$) and $Re = 300$ (same descriptions as in figure 10).

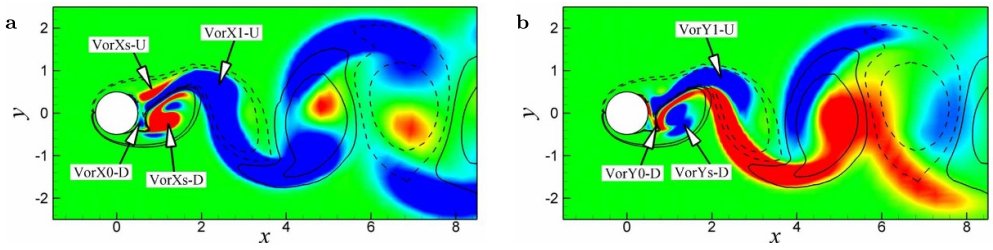

Figure 21. Colour contours of (a) ω_x and (b) ω_y at $z = 0.5$, $t = 931.5$ (T_3) and $Re = 300$ (same descriptions as in figure 10).

originates from that generated on the lower and rear surface, also under the stretching effect of the formed spanwise vortex in the upper shear layer. 'VorY0_U' at T_2 also evolves from that at T_1.

These results all suggest that the formation of streamwise and vertical vorticities in the shear layers in (pure) mode B is more complicated than that in (pure) mode A (Lin *et al* 2019b).

3.3.3. In the FDW. In FDW, the problem is analysed in detail. For the origin of the dominant ω_x in the shear layers, considering a whole cycle, as shown in figures 19(a), 20(a), 21(a) and 22(a), we note a phenomenon: the upstream 'head' of $-|\omega_x|$ always remains at $x \sim 0.8$, and increasing strength at T_2 and T_4, appears near the wake centre. Based on previous analysis, this result can not be explained only by coupled mechanisms, including the vorticity originating from the rear surface just appearing in a certain period (e.g. T_1 and T_3), the stretching of spanwise vortices formed in the shear layers due to inertial forces and the viscous dissipation

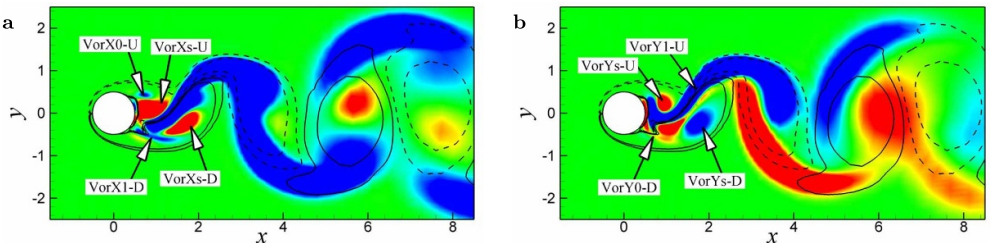

Figure 22. Colour contours of (a) ω_x and (b) ω_y at $z = 0.5$, $t = 932.5$ ($\lesssim T_4$) and $Re = 300$ (same descriptions as in figure 10).

and diffusion. With the help of the vortex-induction mechanism mentioned above and the first sign law, the intensification of $-|\omega_x|$ in 'VorX1_U' at T_2 could be attributed to the induction of $-|\omega_y|$ originating from the lower and rear surface and stretching upward in figure 20(b), while the increasing $-|\omega_x|$ in 'VorX1_D' at T_4 could be attributed to the induction of $+|\omega_y|$ originating from the upper and rear surface and stretching downward in figure 22(b). It is also examined that 'VorX0_D' initially appears at an earlier time T_S between T_1 and T_2, while 'VorX0_U' appears at $T_E \in (T_3, T_4)$, e.g. $843 < T_S < 843.5$ here. Therefore, the streamwise vorticity in the shear layers first originates from that generated on cylinder surfaces but intensifies mainly through the induction of vertical vorticity on surfaces for (pure) mode B, which is obviously different from (pure) mode A (Lin *et al* 2019b). Such a coupled mechanism responsible for the origin of streamwise vortices in (pure) mode B is also different from that in the shear layers and near wake, e.g. the hyperbolic instability of the braid shear layer (Wu and Ling 1993, Williamson 1996a, 1996b, Luo *et al* 2003, Jiang *et al* 2016, 2018), and the vertical instability in the spanwise direction (Agbaglah and Mavriplis 2017).

Consequently, as an example, we obtain the following formation process of streamwise vortices:

(a) $-|\omega_x|$ of 'VorX0_D' in the lower shear layer first appears, originating and stretching from that on the lower and rear surface at $t = T_S$ ($<T_2$).
(b) Then, 'VorX0_D' increases as time proceeds until $t = T_{SE}$ ($<T_3$), as shown in figure 20(a).
(c) After $t = T_{SE}$, e.g. $931 < T_{SE} < 931.5$ here, as shown in figure 21(a), the further intensified 'VorX0_D' begins to gain $-|\omega_x|$ from that on the upper and rear surface.
(d) When $t = T_E$ ($<T_4$), 'VorX0_D' is separated by $+|\omega_x|$ generated on the lower and rear surface, as shown in figure 22(a). 'VorX0_D' becomes 'VorX1_D', which primarily obtains $-|\omega_x|$ induced by $+|\omega_y|$ stretching from that on the upper and rear surface until $t = T_{ES}$ ($<T_1$).
(e) Meanwhile, at $t = T_E$, 'VorX0_U' initially appears because of $-|\omega_x|$ shed from the upper and rear surface.
(f) Finally, in the rest of the cycle (T_{ES}, T_S), 'VorX1_D' is shed along with anticlockwise spanwise vortex, as shown in figure 19(a), until the new 'VorX0_D' appears at $t = T_S$.

The origin of ω_y in the shear layers is also obtained in brief. Further verified by the arrow for dominant $+|\omega_y|$, 'VorY0_D' in figure 21(b) as the origin of ω_y in the lower shear layer, i.e. 'VorY1_D', first appears at T_{SE} and only stretches from that generated on the upper and rear surface during a half cycle (T_{SE}, T_{ES}). At $t = T_{ES}$, 'VorY0_D' is separated by $-|\omega_y|$ generated on the rear surface, and then, it evolves into 'VorY1_D'. In the subsequent half period (T_{ES}, T_{SE}), 'VorY1_D' is intensified, dominantly by the vortex-induction mechanism of $-|\omega_x|$

on the lower and rear surface, and associated with its holding position of $x \sim 0.6$, which is almost invariant in figure 19(b) or 20(b). This could also be due to the coupled stretching effect of $\pm|\omega_z|$ formed in the shear layers and recirculation region near the wake centre. Finally, it is shed at $t = T_{SE}$, and a new 'VorY0_D' is formed. It should be mentioned that the above stretching results in 'VorY1_D' mainly being distributed in the vortex braid of the shedding spanwise vortex with a negative sign at T_{SE}, although 'VorY1_D' originally appears in the lower shear layer.

In summary, the mechanisms for origin of ω_x and ω_y are the initial vortex generation on the wall and then the vortex induction dominantly just behind the body. They are all closely related to the formation and shedding process of spanwise vortices. For example, figures 20(a) and 21(a) illustrate that 'VorX0_D' is stretched mainly by $+|\omega_z|$, while 'VorY0_D' is stretched dominantly by $+|\omega_z|$ in figures 21(a) and 22(a) at different time periods.

3.4. *Features of subordinate* ω_x and ω_y *in FDW*

In FDW, some features are also found out for the subordinate streamwise and vertical components of the vorticity with specific signs opposite to those of the dominant ω_x and ω_y, denoted by 'VorXs_U' and 'VorXs_D' in figure 19(a) and 'VorYs_U' and 'VorYs_D' in figure 20(b), respectively, in the shear layers. The magnitudes of these subordinate ω_x and ω_y are minor. The formation process for subordinate ω_x is very similar to that for dominant ω_x in (pure) mode A, but with a shorter formation period. The physical origin of such subordinate ω_x could also be interpreted by the present vortex-induction mechanism. For example, $+|\omega_x|$ in 'VorXs_D' is first induced by $-|\omega_y|$ on the lower and rear surface at T_{ES}, and increases until $t = T_S$, as shown in figure 14(a) or 19(a). Then, it is further intensified by $+|\omega_x|$ not only generated on the upper and rear surface but also induced by $-|\omega_y|$ on the lower and rear surface, as shown in figure 13 or 20, over the time period of T_S to T_{SE}. Finally, it is shed downstream into the near wake in the rest of the half cycle (T_{SE}, T_{ES}), associated with the similar formation process of 'VorXs_U' in the upper shear layer, as shown in figures 21(a) and 22(a).

However, the formation of subordinate ω_y is completely different from that of dominant ω_y in (pure) mode A or B. For instance, $-|\omega_y|$ in 'VorYs_D' is initially induced by the above $+|\omega_x|$ in 'VorXs_D' at the time between T_1 and T_2 or at approximately T_S, as shown in figures 19(b) and 20(b), which indicates that there is a phase difference in the time between the appearance of subordinate ω_x and ω_y. Such a vortex-induction mechanism is valid until the shedding of 'VorXs_D' at $t = T_{SE}$. Then, 'VorYs_D' and 'VorXs_D' are shed synchronously, as shown in figures 21(b) and 22(b).

According to the analysis of the vorticity signs of these subordinate ω_x and ω_y, the two sign laws mentioned before also prevail in the present circumstances.

3.5. *Pure mode B: redescription, formation and whole shedding process*

According to the second sign law, (pure) mode B in figures 17 and 18 can be redescribed by the Π_- and Π_+ vortices, defined in previous works (Lin *et al* 2018, 2019b), alternately shed out of phase across the span when $\lambda = \lambda_B$. The vortical structure in (pure) mode B is just opposite to that in (pure) mode A (Lin *et al* 2018, 2019b), in which the Π_- and Π_+ vortices with specific wavelengths are alternately shed in phase across the span. Moreover, the second sign law provides indirect proof that there are two and only two types of 3D vortex-shedding modes in the natural laminar wake transition of a bluff body, as reported in previous work (Lin *et al* 2018), because there are two and only two groups of vorticity sign combinations of the three vorticity components appearing in the upper and lower shear layers.

Table 2. Summary of the formation and shedding process of streamwise and vertical vorticities in the upper ($y>0$) and lower ($y<0$) shear layers in a whole cycle of (pure) mode B, associated with alternately shedding spanwise vortices with vorticity $\pm|\omega_z|$, at $Re=300$, where 'Ap', 'In' and 'Sh' in brackets denote the vorticity that initially appeared, increased and were shed, respectively, and symbol $\mapsto$ indicates the transformation or evolution process.

	Time T_S	$T_S \to T_2 \to T_{SE}$	T_{SE}	$T_{SE} \to T_3 \to T_E$
$y>0$	VorX0_U $\mapsto$ VorX1_U	VorX1_U(In)	VorX1_U(Sh)	VorX1_U(Sh)
	VorY0_U(In)	VorY0_U(In)	VorY0_U $\mapsto$ VorY1_U	VorY1_U(In)
	$-\|\omega_z\|$(In)	$-\|\omega_z\|$(In)	$-\|\omega_z\|$(Sh)	$-\|\omega_z\|$(Sh)
y<0	VorX0_D(Ap)	VorX0_D(In)	VorX0_D(In)	VorX0_D(In)
	VorY1_D(In)	VorY1_D(In)	VorY0_D(Ap), VorY1_D(Sh)	VorY0_D(In)
	$+\|\omega_z\|$(Sh)	$+\|\omega_z\|$(Sh)	$+\|\omega_z\|$(In)	$+\|\omega_z\|$(In)
	Time T_E	$T_E \to T_4 \to T_{ES}$	T_{ES}	$T_{ES} \to T_1 \to T_S$
$y>0$	VorX0_U(Ap)	VorX0_U(In)	VorX0_U(In)	VorX0_U(In)
	VorY1_U(In)	VorY1_U(In)	VorY0_U(Ap), VorY1_U(Sh)	VorY0_U(In)
	$-\|\omega_z\|$(Sh)	$-\|\omega_z\|$(Sh)	$-\|\omega_z\|$(In)	$-\|\omega_z\|$(In)
y<0	VorX0_D $\mapsto$ VorX1_D	VorX1_D(In)	VorX1_D(Sh)	VorX1_D(Sh)
	VorY0_D(In)	VorY0_D(In)	VorY0_D $\mapsto$ VorY1_D	VorY1_D(In)
	$+\|\omega_z\|$(In)	$+\|\omega_z\|$(In)	$+\|\omega_z\|$(Sh)	$+\|\omega_z\|$(Sh)

Consequently, the formation and shedding process of (pure) mode B in a whole cycle can be briefly described as in table 2. It clearly demonstrates that ω_x and ω_y on the same side of the shear layer initially appear with a phase difference of approximately $(T_{ES}-T_E)$ or $(T_{SE}-T_S)$ but shed out of phase over time. As for the formation process before shedding, the streamwise vorticity of one sign experiences approximately three quarters of a cycle, e.g. $t\in(T_S,T_{ES})$, while the vertical vorticity lasts for a whole cycle.

3.6. Other physical relationships or differences between (pure) modes A and B

3.6.1. Vorticity sign of shedding vortices. Two sign laws are summarized. The first sign law shows the intrinsic relationship between ω_x and ω_y, precisely in region R-I and dominantly in regions R-II and R-III, written as

$$\mathrm{sgn}(\omega_x\cdot\omega_y)=\begin{cases}-1, & \text{if } y<0,\\ 1, & \text{if } y>0.\end{cases} \tag{4}$$

The second sign law indicates the sign relationship between additional vorticities and the spanwise vorticity, also exactly in R-I, dominantly in R-II and theoretically in R-III, written as

$$\mathrm{sgn}(\omega_x\cdot\omega_y\cdot\omega_z)=-1. \tag{5}$$

3.6.2. Sign symmetry of the surface vorticity. Two types of sign symmetry of dominant surface vorticities at the same spanwise position are illustrated in CT-3 and FDW. Particularly,

for the second sign symmetry appearing in FDW, for the convenience, the attention is placed on the rear surface (except near the wake centre $y = 0$), and only the Fourier mode of $n = 1$ is analysed. As previously reported for (pure) mode A (Lin *et al* 2019b), $\mathrm{sgn}(\omega_x)$ on the upper side is always the same as that on the lower side, while $\mathrm{sgn}(\omega_y)$ is opposite on the upper and lower sides. This means that the symmetry of the surface vorticity is opposite to that of the vorticity in the shear layers or near wake, where ω_x with opposite signs in the upper and lower shear layers occurs, but ω_y with a single sign occurs in both shear layers.

Similarly, this phenomenon is also discovered in (pure) mode B, as shown in figure 17. $\mathrm{sgn}(\omega_x)$ on the rear surface is anti-symmetric about $y = 0$, while ω_x with a single sign is shed at the same spanwise position. However, $\mathrm{sgn}(\omega_y)$ is symmetric about $y = 0$, but ω_y with opposite signs is alternately shed.

Such a feature, different sign symmetries of additional vorticities on the rear surface and in the shear layers, is believed to be closely related to the generation and formation of vorticity. This further indicates that the mechanism of vorticity generation on the wall is not sufficient to interpret the physical origin of additional vorticities in the shear layers because the sign of the vorticity on one side of rear surface is always opposite to that on the same side of the shear layers. It could be associated with the sign laws on the rear surface just behind the body, which will be investigated in the future.

3.6.3. Wavy spanwise vortices. In previous studies (Meiburg and Lasheras 1988, Lin *et al* 2018), two types of interactions with spanwise vortices, referred to as streamwise and vertical interactions, were identified. Both of them can be used to explain the wavy spanwise vortex. There is a relationship between their vorticity signs. For (pure) mode A with spatial symmetry of additional vortices with ω_x and ω_y in the near wake, distorted spanwise vortices can be explained by the dominant vertical interaction between vertical and spanwise vortices. The physical reason is attributed to the enhancement effect from superimposed vertical vorticies with a single sign that are shed from shear layers and mainly appear in the vortex core. In contrast, the cancelation effect between the opposite-signed streamwise vorticies, which are easily convected into the core of the upstream spanwise vortex, leads to the streamwise interaction between streamwise and spanwise vortices being weak.

Therefore, the more uniformly shedding spanwise vortices in (pure) mode B can be similarly newly interpreted. Typically, as shown in figure 18 or 22, dominant additional vorticities in the near wake are almost distributed in vortex braids, rather than vortex cores. Another factor may be that the spanwise vortices or vortex cores in (pure) mode B are stronger than those in (pure) mode A due to the higher shear rate and less viscous dissipation at $Re = 300$. Moreover, vertical vortices with opposite signs have the cancelation effect on the same spanwise vortex. Therefore, the vertical interaction would be weak. Streamwise vortices with a single sign are mainly distributed across the borders of opposite-signed spanwise vorticities near the wake centre and almost shed at one side of vortex braids, e.g. as in figure 22(a), instead of at vortex cores. Similarly, the enhancement effect of these superimposed streamwise vortices leads to vortex braids being wavy, e.g. as in figure 18(c). Thus, the streamwise interaction is dominant in vortex braids.

4. Conclusions

The second 3D wake instability, i.e. (pure) mode B, is investigated. DNS of the flow past a circular cylinder is mainly performed at $Re = 300$ and $L_Z = \lambda_B = 1$.

Through the analysis of the force histories and frequency, three flow stages are identified, i.e. the CT, the IS and the FDW flow. In CT, the wake flow mainly evolves from the initial still flow into two-dimensional spanwise vortices that are alternately shed. As for IS, the basic characteristics of mode B appear, although the shedding spanwise vortices still appear to be two-dimensional.

From the viewpoint of the specific vorticity sign, (pure) mode B can be described by streamwise vorticies with the same sign parallel to each other along the streamwise direction between two neighbouring vortex braids and the vertical vortices with opposite signs in a staggered arrangement, associated with alternately shedding spanwise vortices with opposite signs.

The spatio-temporal evolution of the vorticity shows that additional vorticities appear almost throughout the whole computational time. Over time, they first appear very early compared to those in the IS. Then, they are gradually enhanced to a certain level in the FDW. As for the spatial features, these additional vorticities initially appear on cylinder surfaces due to the intrinsic 3D instability, which confirms that the three dimensionality of the present flow first occurs near solid walls, instead of in the shear layers or near wake, regardless of (pure) modes A and B.

Based on careful comparisons of the sign evolution of the three vorticity components distributed in three sub-regions, the two sign laws discovered in (pure) mode A (Lin *et al* 2019b) also exist in the present (pure) mode B. Based on the second sign law, (pure) mode B could be redescribed by the Π_- and Π_+ vortices alternately shed out of phase across the span. Regarding the physical origin of the streamwise or vertical vorticity in the shear layers, the mechanism is mainly attributed to the vortex generation on the wall first and then the dominant vortex induction behind the body.

During the whole shedding cycle, ω_x and ω_y on the same side of the shear layers initially appear with a phase difference but are shed out of phase over time.

As a new feature, a special sign symmetry of the surface vorticity on the rear surface opposite to that in the near wake for both (pure) modes A and B is observed.

In addition, for (pure) mode B, the streamwise interaction is dominant, leading to the vortex braids, rather than the vortex cores, wavily varying. In (pure) mode A, the vertical interaction is relatively dominant for the wavy spanwise vortex.

Moreover, for subordinate ω_x and ω_y in the FDW, the two sign laws are also effective. In particular, the physical origin and formation process have their own features, different from those of the dominant vorticities in (pure) mode B.

In the future, as subsequent parts of the study, the spatio-temporal evolution of the vorticity in large-scale vortex dislocations will be investigated at $Re = 200 \sim 300$ with a large computational spanwise length of 12.

Acknowledgment

This work was financially supported by the Strategic Priority Research Program of the Chinese Academy of Science (Grant No. XDB22030101).

Appendix. Effects of the Reynolds number and the spanwise grid size

A1. Effect of the Reynolds number on the sign laws at Re $=$ *310 and 320*

Typically, at $t = T_2$, as shown in figures A1 and A2 at $Re = 310$ and figures A3 and A4 at $Re = 320$, the distributions of dominant vorticities with specific signs show that the vorticity

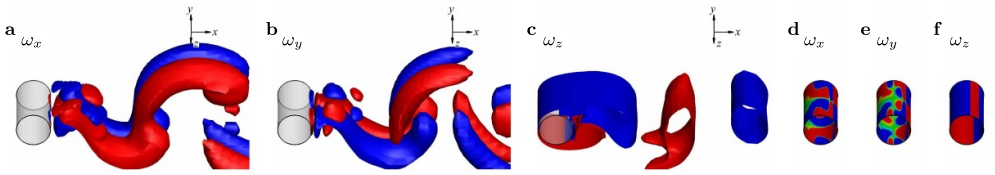

Figure A1. At $t = 896$ (T_2), iso-surfaces of (a) $\omega_x = \pm 0.2$, (b) $\omega_y = \pm 0.2$ and (c) $\omega_z = \pm 1$, and contours of (d) ω_x, (e) ω_y and (f) ω_z on cylinder surfaces at $Re = 310$ (same descriptions as in figure 5).

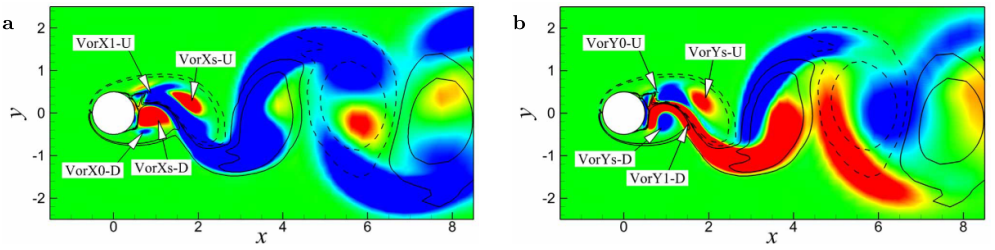

Figure A2. Colour contours of (a) ω_x and (b) ω_y at $z = 0.25$, $t = 896$ (T_2) and $Re = 310$ (same descriptions as in figure 10).

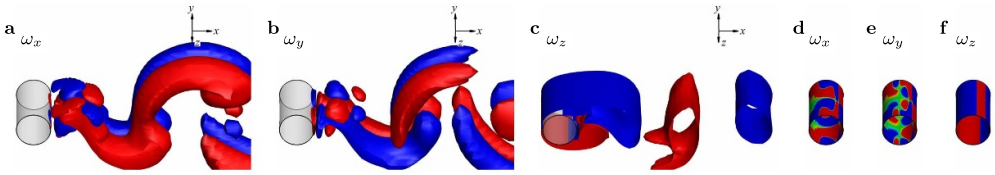

Figure A3. At $t = 765$ (T_2), iso-surfaces of (a) $\omega_x = \pm 0.2$, (b) $\omega_y = \pm 0.2$ and (c) $\omega_z = \pm 1$, and contours of (d) ω_x, (e) ω_y and (f) ω_z on cylinder surfaces at $Re = 320$ (same descriptions as in figure 5).

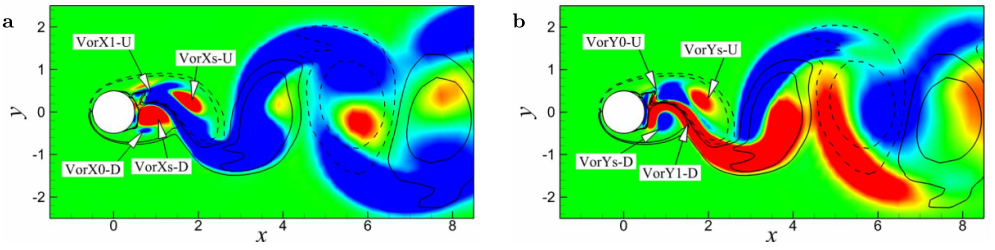

Figure A4. Colour contours of (a) ω_x and (b) ω_y at $z = 0.25$, $t = 765$ (T_2) and $Re = 320$ (same descriptions of figure 10).

sign relationships are qualitatively consistent with those at $Re = 300$, as are the physical mechanisms of the appearance of ω_x and ω_y in the shear layers, even with the appearance of Fourier mode of $n = 2$ on cylinder surfaces. Therefore, for (pure) mode B, the two sign laws and

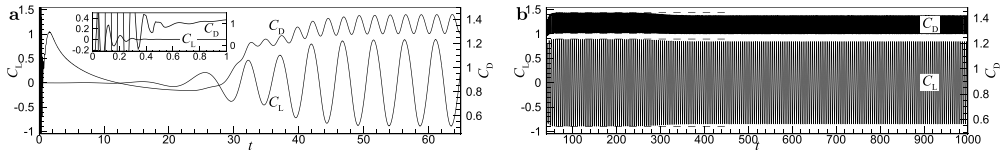

Figure A5. When $\Delta z = 0.05$, time histories of C_D and C_L for (pure) mode B at $Re = 300$, typically (a) the CT, $t \in (0, 55)$, along with a small window at $t < 1$, (b) the IS, $t \in (55, 380)$, and the FDW, $t > 380$. In sub-figure (b), horizontal dashed lines denote the peak-to-peak amplitudes of forces at the first IS.

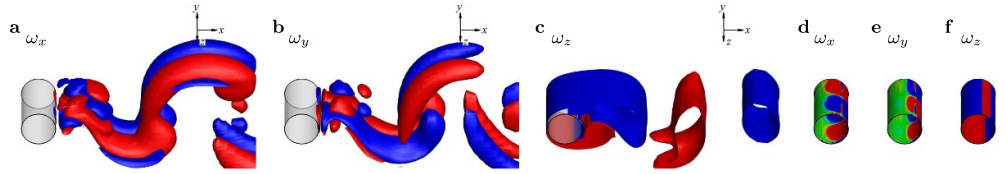

Figure A6. When $\Delta z = 0.05$, iso-surfaces of (a) $\omega_x = \pm 0.2$, (b) $\omega_y = \pm 0.2$ and (c) $\omega_z = \pm 1$, and contours of (d) ω_x, (e) ω_y and (f) ω_z on cylinder surfaces at $t = 864.5$ (T_2) and $Re = 300$ (same descriptions as in figure 5).

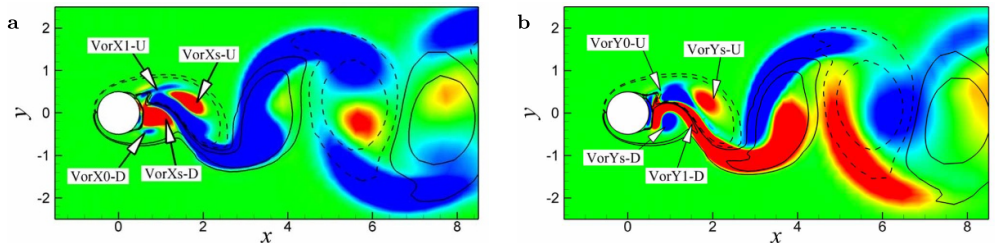

Figure A7. When $\Delta z = 0.05$, colour contours of (a) ω_x and (b) ω_y at $z = 0.18$, $t = 864.5$ (T_2) and $Re = 300$ (same descriptions as in figure 10).

physical origin of dominant ω_x and ω_y, as well as the whole formation-shedding process, even for subordinate ω_x and ω_y, are independent of the Reynolds number.

A2. Effect of Δz *=0.05 on the vorticity evolution at* Re $=$ *300*

As for the effect of the spanwise grid size, a calculation with $\Delta z = 0.05$ is performed at $Re = 300$. As shown in figure A5, there are also three main stages identified in the time histories of the fluid forces, qualitatively consistent with those when $\Delta z = 0.1$. For example, the entire CT first appears when $t < 55$. Then, the flow evolves into the IS when $55 < t < 380$. Among them, the first sub-stage at $t < 260$ is associated with constant force amplitudes, while the second at $t > 260$ is associated with the amplitudes reducing almost linearly. Such special behaviours of fluid forces before FDW are also found at $Re = 310$ and 320 with $\Delta z = 0.1$, and similar to those in (pure) mode A (Lin *et al* 2019b). Finally, the wake flow is fully developed at $t > 380$, also with invariable amplitudes, which are slightly less than those in the first IS. In FDW, we have: $\overline{C}_D = 1.3497$ and $C'_L = 0.5949$ which are slightly less than those with $\Delta z = 0.1$, and $St = 0.2085$ with $\delta f = 1.7 \times 10^{-3}$.

However, typically, as shown in figure A6 at $t = 864.5$ (T_2), the sign relationships still agree well with those at $\Delta z = 0.1$, as does the physical origin of ω_x and ω_y, as shown in figure A7. Consequently, this means that the smaller spanwise grid size also has no qualitative effect on the evolution of the vorticity and its sign, particularly for the physical origin of dominant and subordinate ω_x and ω_y in the shear layers.

ORCID iD

Z R Tan https://orcid.org/0000-0002-9456-0521

References

Agbaglah G and Mavriplis C 2017 Computational analysis of physical mechanisms at the onset of three-dimensionality in the wake of a square cylinder *J. Fluid Mech.* **833** 631–47
Agbaglah G and Mavriplis C 2019 Three-dimensional wakes behind cylinders of square and circular cross-section: early and long-time dynamics *J. Fluid Mech.* **870** 419–32
Barkely D and Henderson R D 1996 Three-dimensional Floquet stability analysis of the wake of a circular cylinder *J. Fluid Mech.* **322** 215–41
Barkley D, Tuckerman L S and Golubitsky M 2000 Bifurcation theory for three-dimensional flow in the wake of a circular cylinder *Phys. Rev.* E **61** 5247–52
Brede M, Eckelmann H and Rockwell D 1996 On secondary vortices in the cylinder wake *Phys. Fluids* **8** 2117–24
C.H.K. Williamson 1996 Vortex dynamics in the cylinder wake *Annu. Rev. Fluid Mech.* **28** 477–539
Darekar R M and Sherwin S J 2001 Flow past a square-section cylinder with a wavy stagnation face *J. Fluid Mech.* **426** 263–95
Henderson R D 1997 Nonlinear dynamics and pattern formation in turbulent wake transition *J. Fluid Mech.* **352** 65–112
Jiang H Y, Cheng L and An H W 2018 Three-dimensional wake transition of a square cylinder *J. Fluid Mech.* **842** 102–27
Jiang H and Cheng L 2019 Transition to the secondary vortex street in the wake of a circular cylinder *J. Fluid Mech.* **867** 691–722
Jiang H, Cheng L, Draper S and An H 2017 Prediction of the secondary wake instability of a circular cylinder with direct numerical simulation *Comput. Fluids* **149** 172–80
Jiang H, Cheng L, Draper S, An H and Tong F 2016 Three-dimensional direct numerical simulation of wake transitions of a circular cylinder *J. Fluid Mech.* **801** 353–91
Karniadakis G E and Triantafyllou G S 1992 Three-dimensional dynamics and transition to turbulence in the wake of bluff bodies *J. Fluid Mech.* **238** 1–30
Leweke T and Williamson C H K 1998 Three-dimensional instabilities in wake transition *Eur. J. Mech.* B **17** 571–86
Lin L M, Ling G C and Wu Y X 2010 Mechanism responsible for the complete suppression of Kármán vortex in flows past a wavy square-section cylinder *Chin. Phys. Lett.* **27** 034702
Lin L M, Shi S Y and Wu Y X 2018 Intrinsic relationship of vorticity between modes A and B in the wake of a bluff body *Theor. Appl. Mech. Lett.* **8** 320–5
Lin L M, Shi S Y and Wu Y X 2019 Physcial mechanism for origin of streamwise vortices in mode A of a square-section cylinder *Acta Mech. Sin.* **35** 411–8
Lin L M, Shi S Y, Zhong X F and Wu Y X 2019 Mechanism of wavy vortex and sign laws in flow past a bluff body: vortex-induced vortex *Acta Mech. Sin.* **35** 1–14
Lin L M and Tan Z R 2019 DNS in evolution of vorticity and sign relationship in wake transition of a circular cylinder: (pure) mode A *Acta Mech. Sin.* **35** 1131–49
Lin L M and Wu Y X 2020 Mechanism for vorticity in a secondary flow within a pipe: vortex-induced vortex *Phys. Fluids* **32** 033602
Lin L M, Zhong X F and Wu Y X 2018 Effect of perforation on flow past a conic cylinder at $Re = 100$: wavy vortex and sign laws *Acta Mech. Sin.* **34** 812–29
Ling G C and Chang Y 1999 Three-dimensional stability analysis of the periodic wake behind a circular cylinder by low-dimensional Galerkin method *Chin. J. Theor. Appl. Mech.* **31** 652–60

Luo S C, Chew Y T and Ng Y T 2003 Characteristics of square cylinder wake transition flows *Phys. Fluids* **15** 2549–59
Meiburg E and Lasheras J C 1988 Experimental and numerical investigation of the three-dimensional transition in plane wakes *J. Fluid Mech.* **190** 1–37
Persillon A and Braza M 1998 Physical analysis of the transition to turbulence in the wake of a circular cylinder by three-dimensional Navier–Stokes simulation *J. Fluid Mech.* **365** 23–88
Posdziech O and Grundmann R 2001 Numerical simulation of the flow around an infinitely long circular cylinder in the transition regime *Theor. Comput. Fluid Dyn.* **15** 121–41
Rao A, Thompson M C, Leweke T and Hourigan K 2013 The flow past a circular cylinder translating at different heights above a wall *J. Fluids Struct.* **41** 9–21
Sheard G J, Thompson M C and Hourigan K 2003 A coupled Landau model describing the Strouhal–Reynolds number profile of a three-dimensional circular cylinder wake *Phys. Fluids* **15** L68–L71
Thompson M C, Leweke T and Williamson C H K 2001 The physical mechanism of transition in bluff body wakes *J. Fluids Struct.* **15** 607–16
Williamson C H K 1996 Three-dimensional wake transition *J. Fluid Mech.* **328** 345–407
Wu Z B and Ling G C 1993 Numerical study on the mechanism for three-dimensional evolution of vortex and the structural features in the wake behind a circular cylinder *Chin. J. Theor. Appl. Mech.* **25** 264–75
Yokoi Y and Kamemoto K 1992 Initial stage of a three-dimensional vortex structure existing in a two-dimensional boundary layer separation flow (observation of laminar boundary layer separation over a circular cylinder by flow visualization) *JSME Int. J.* II **35** 189–95
Yokoi Y and Kamemoto K 1993 Initial stage of a three-dimensional vortex structure existing in a two-dimensional boundary layer separation flow (visual observation of laminar boundary layer separation over a circular cylinder from the side of a separated region) *JSME Int. J.* B **36** 201–6